Journal of Membrane Science & Research

journal homepage: www.msrjournal.com

Research Paper

Impacts of Shaft on Mass Transfer in a Reverse Osmosis Rotating Disk Membrane

Choo Er Joey Vei [1], Khai Ching Ng [3], Yie Kai Chong [1], Jia Xin Tan [1], Woei Jye Lau [4], Yong Yeow Liang [1, 2, *]

[1] *Faculty of Chemical and Process Engineering Technology, Universiti Malaysia Pahang Al-Sultan Abdullah, Lebuh Persiaran Tun Khalil Yaakob, 26300, Kuantan, Pahang, Malaysia*
[2] *Centre for Research in Advanced Fluid and Processes, Universiti Malaysia Pahang Al-Sultan Abdullah, Lebuh Persiaran Tun Khalil Yaakob, 26300, Kuantan, Pahang, Malaysia*
[3] *University of Nottingham Malaysia, Jalan Broga, 43500 Semenyih, Selangor, Malaysia*
[4] *Advanced Membrane Technology Research Center, Faculty of Chemical and Energy Engineering, Universiti Teknologi Malaysia, 81310 Skudai, Johor, Malaysia*

Article info

Received 2024-05-28
Revised 2024-10-01
Accepted 2024-10-01
Available online 2024-10-01

Keywords

Rotating disk
Shaft
Reverse osmosis
Stirring
Mass transfer
Wall shear stress

Highlights

- Case without shaft outperform those with shaft at high rotational speed
- Results show uniform flow with shaft while non-uniform flow without shaft
- Rotational direction insignificantly influences $\overline{\gamma}_{,ave}$, $\overline{k}_{mt,ave}$ and $\overline{J}_{,ave}$.
- Smaller gap between disk and membrane causes smaller stagnation zone and larger k_{mt}.

Graphical abstract

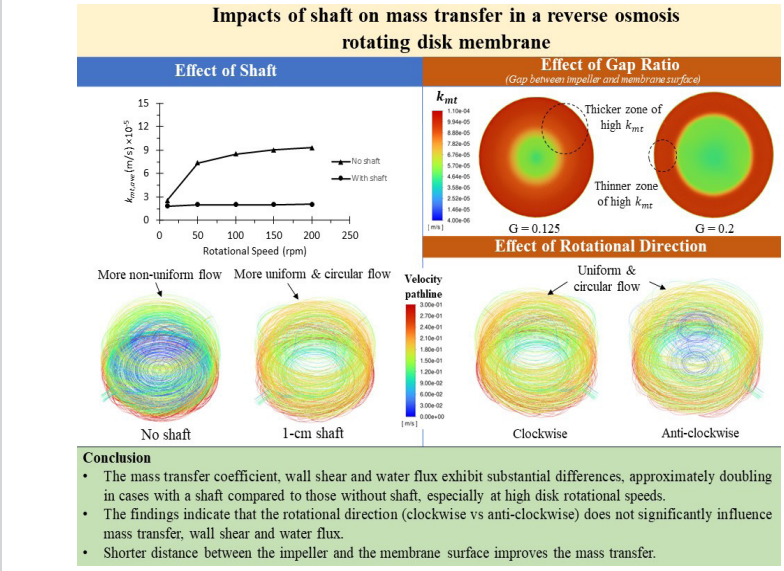

Abstract

A rotating disk has been proposed for integration within the membrane module due to its ability to induce shear near the membrane. This study focuses on the hydrodynamics and mass transfer simulation of a reverse osmosis (RO) rotating disk membrane system using three-dimensional computational fluid dynamics techniques. The mass transfer coefficient ($\overline{k}_{mt,ave}$), wall shear ($\overline{\gamma}_{,ave}$) and water flux ($\overline{J}_{,ave}$) show significant deviations of at least double between cases with and without a shaft (at high disk rotational speed). This is because at a higher disk rotational speed, the flow for the case with shaft experiences a more uniform and exhibits circular velocity pathline caused by the high-speed circulating shaft, whereas a more non-uniform flow is obtained for the case without shaft. The significance of non-uniform flow lies in its ability to enhance the flow perpendicular to the membrane surface. This enhancement is evidenced by the stronger turbulent kinetic energy observed near the membrane surface when the shaft is absent especially at a higher disk rotational speed. The results also indicate that rotational direction (clockwise vs. anticlockwise) does not significantly impact $\overline{\gamma}_{,ave}$, $\overline{k}_{mt,ave}$ and $\overline{J}_{,ave}$. Regarding the geometrical effect, it was found that reducing the gap between the membrane interface layer and the impeller decreases the size of the quiescent region near the membrane surface. This reduction results in stronger mixing near the membrane, which enhances mass transfer and increases water flux.

* Corresponding author: yongyeow.liang@umpsa.edu.my (Y.Y.Liang)

DOI: 10.22079/jmsr.2024.2030505.1666

1. Introduction

Membrane technology has become increasingly important in process industries due to its environmental friendliness, cost-effectiveness, and application flexibility [1, 2]. It is widely used in fields such as pharmaceuticals, wastewater treatment, food processing, and petroleum refining [3]. However, concentration polarization (CP) appears as a drawback in the membrane separation system which limits the permeate flux and the separation efficiency [4]. CP occurs due to the membrane rejection and accumulation of solute near the membrane surface, thereby leading to the water flux decline. This can subsequently cause membrane fouling, where rejected particles accumulate and form a cake layer on the surface of the membrane. These issues result in reduced separation efficiency, higher maintenance costs, and shorter membrane lifespan.

One way to minimize CP is by introducing agitation or stirring into the system [5]. Stirring disrupts the boundary layer on the membrane surface and increases the permeate flux. A rotating disk or impeller can be incorporated into the membrane module to generate shear forces that enhance mixing near the membrane surface. Stirred-membrane modules are generally proposed for small to medium-scale applications [3]. There are several designs for this type of module, namely rotating disk (RD) [6] and vibratory shear enhanced process (VSEP).

Computational fluid dynamic (CFD) has been extensively used to study the local hydrodynamic and mass transport behavior of a membrane process [7-9]. Although the effects of stirring have been widely explored in the literature [10-12], there is limited research on how stirring impacts mass transfer at the membrane surface. It shall be noted that most CFD studies within membrane applications only consider membrane modules such as hollow fiber [13], plate and frame [14] or spiral wound. To our understanding, only one study by Park et al. has investigated the impact of impeller geometry on area-averaged flux. They examined a wheel-type impeller and studied how the number of wheel-shaped patterns affected flux [15]. An excellent review of dynamic membrane filtration was provided by Jaffrin [7] who has discussed the fundamentals of operation and fluid dynamics in rotating systems and the generation of Taylor vortices using rotating parts. Rotational speed was found as the most influential parameter to determine the flow pattern, mass transfer and shear rate. Higher rotational speed contributes to enhanced flux, but it comes with the cost of heat dissipation and higher power utilities [16].

To our understanding, only a handful of research has studied the impact of shaft on mixing [17, 18]. Past literature [17] indicates that positioning a rotating disk at an eccentric location between 24% and 48% of the vessel's diameter, and at one-third of the vessel's height, may yield optimal mixing characteristics. With respect to rotational direction, it was shown that opposite clockwise rotational direction minimizes energy consumption [18]. Another study was conducted by Wang, Wu and Ohmura [18] which indicates that systems with shafts inclined by greater than or equal to 20°, can significantly improve mixing quality and decrease mixing duration. With higher shaft angles, greater power input is needed; however, the mixing time is reduced. Nonetheless, its effect on mixing and mass transfer near the membrane surface remains unexplored. It is anticipated that the shorter distance between the rotating disk and the membrane surface would lead to higher mass transfer. This phenomenon is similar to observations in spacer-filled channels, where the distance between the membrane surface and spacer has been found to impact mass transfer [19]. Nevertheless, the extent to which mass transfer is enhanced by reducing the gap between the membrane surface and impeller is currently unclear.

This paper aims to elucidate the mass transfer mechanism induced by stirring. It explores how the shaft influences hydrodynamic behavior on the membrane surface, whether rotational direction plays a significant role in enhancing membrane surface mass transfer, and how the gap between the membrane surface and the impeller affects mass transfer. The following sections address these questions.

2. Methodology

2.1. Geometry development and simulation conditions

The three-dimensional (3D) geometry under consideration is a circular tank with an inlet and outlet as shown in Fig. 1. The dimension of the tank is set following the typical industrial design used in food processing applications [3, 6, 20, 21]. To study the mixing effect, a circular disk or impeller was employed in the circular tank to create a circular motion as shown in Fig. 1. The disk is rotating in the y-direction along the center point of the tank using the sliding mesh approach (as discussed in Section 2.3). The dimension of the rotating disk membrane tank is summarized in Table 1.

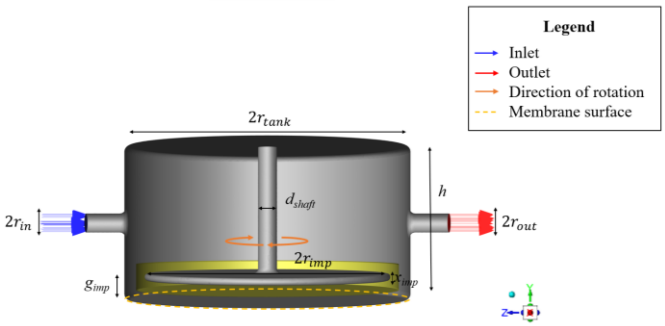

Fig. 1. Schematic diagram of the membrane module with rotating disk.

Table 1
Dimension of the membrane module.

Parameter	Dimension (m)
Tank Height (h)	0.08
Tank Radius (r_{tank})	0.075
Impeller Radius (r_{imp})	0.0645
Impeller Thickness (x_{imp})	0.0035
Shaft Diameter (d_{shaft})	0.01
Inlet Radius (r_{in})	0.005
Outlet Radius (r_{out})	0.005
Gap (g_{imp})	0.01

The typical stirring speed used in industrial applications is around 50 rpm. Therefore, this paper examines a range of 10 to 200 rpm [22]. The gap ratio is defined as the distance between the membrane surface and the impeller divided by the tank height ($G = g_{imp}/h$), with gap ratios ranging from 0.125 to 0.2 considered for CFD analysis. The geometries were simulated both with and without a 1 cm shaft. A summary of the impeller rotational speeds and gap ratios is provided in Table 2.

Table 2
Range of rotational speed and gap ratio simulated in this study.

Variables	Range
Rotational speed (n)	10 – 200 rpm
Gap Ratio (G)	0.125 – 0.2

2.2. Model description

In this 3D CFD simulation, constant Newtonian fluid properties were specified in the ANSYS Fluent R1 2022. Reynolds-averaged Navier-Stokes (RANS) equations are employed to compute the fluid flow in the tank. The time-averaged variables are expressed as $\bar{\phi}$. The continuity and RANS equations are expressed as in Equations (1) and (2) respectively.

$$\frac{\partial \bar{u}_i}{\partial x_i} = 0 \tag{1}$$

$$\rho \bar{u}_j \frac{\partial \bar{u}_i}{\partial x_j} = \rho g + \frac{\partial}{\partial x_j}\left[-\bar{p}\delta_{ij} + \mu\left(\frac{\partial \bar{u}_i}{\partial x_j} + \frac{\partial \bar{u}_j}{\partial x_i} \right) - \rho \overline{u'_i u'_j} \right] \tag{2}$$

where the change in mean momentum of fluid due to unsteadiness is balanced by the mean gravitational force (g), the viscous stress, the apparent stress $\left(-\rho \overline{u'_i u'_j}\right)$ due to the fluctuating velocity (u') field and the mean pressure field isotropic stress.

The solute concentration conservation used to solve for 3D mass transfer is shown in Equation (3):

$$\rho \frac{\partial \omega}{\partial t} + \rho\left(\bar{u}_i \frac{\partial \omega}{\partial x_i} + \bar{u}_j \frac{\partial \omega}{\partial x_j} + \bar{u}_k \frac{\partial \omega}{\partial x_k} \right) = \rho D \left(\frac{\partial^2 \omega}{\partial x_i^2} + \frac{\partial^2 \omega}{\partial x_j^2} + \frac{\partial^2 \omega}{\partial x_k^2} \right) \tag{3}$$

where ω refers to solute mass fraction and D refers to solute diffusivity.

The k-ε model was chosen as the turbulent model which has accounted for two transport equations, namely the turbulent kinetic energy (k) in Equation (4) and the viscous dissipation rate of turbulent kinetic energy (ε) in Equation (5).

$$\frac{\partial(\rho k)}{\partial t}+\frac{\partial(\rho k\bar{u}_i)}{\partial x_i}=\frac{\partial}{\partial x_j}\left[\frac{\mu_t}{\sigma_k}\frac{\partial k}{\partial x_j}\right]+2\mu_t E_{ij}E_{ij}-\rho\varepsilon \tag{4}$$

$$\frac{\partial(\rho\varepsilon)}{\partial t}+\frac{\partial(\rho\varepsilon\bar{u}_i)}{\partial x_i}=\frac{\partial}{\partial x_j}\left[\frac{\mu_t}{\sigma_\varepsilon}\frac{\partial \varepsilon}{\partial x_j}\right]+C_{1\varepsilon}\frac{\varepsilon}{k}2\mu_t E_{ij}E_{ij}-C_{2\varepsilon}\rho\frac{\varepsilon^2}{k} \tag{5}$$

where u_i represents velocity component in the corresponding direction and E_{ij} represents the component of rate of deformation while μ_t is the eddy viscosity as described in Equation (6).

$$\mu_t=\rho C_\mu\frac{k^2}{\varepsilon} \tag{6}$$

where the coefficient, C_μ, $C_{1\varepsilon}$, $C_{2\varepsilon}$, σ_k and σ_ε are set as 0.09, 1.44, 1.92, 1.00 and 1.30, respectively [12].

2.3. Boundary condition

The simulation was run using the sliding mesh approach to perform the stirring effect by the rotation of impeller. The sliding mesh method is chosen to simulate rotating flow as it is capable of accurately describing the transient flow caused by rotating flow [23]. The outer and inner domain was generated tdistinguish between stationary and moving domains. The inner domain, in mh motion, was set as the moving part with a rotational speed range from 10 to 200 rpm. The rotating disk was selected as the translational moving wall.

At the inlet, the solute mass fraction was set to 0, and the velocity was 0.11 m/s (Q = 30 L/h). There are two commonly used types of boundary conditions for the membrane surface in CFD, namely permeable wall and impermeable wall membrane [24]. The permeable model couples concentration polarization with water flux, requiring more computational effort than the impermeable model. In the impermeable wall approach, a solute mass fraction value (ω = 0.06) is assigned, and the membrane is treated as a non-slip boundary condition. This solute mass fraction was chosen because it corresponds to a typical value at the membrane surface [24]. Nevertheless, it is worth noting that the mass transfer coefficient computed in the impermeable wall can be used to predict mass transfer under permeation condition through a generalized correction factor [25]. Previous studies have shown that the solute mass fraction at the surface of the membrane does not significantly affect the mass transfer (Sherwood number) at any location, regardless of the specific value used [26]. Thus, the impermeable wall boundary condition for the membrane is used for the simulation study due to its simplicity. The boundary conditions of the membrane tank are tabulated in Table 3.

Table 3
Boundary condition for membrane tank with rotating disk.

Boundary condition	Explanation	Mathematical Expression
Inlet	Velocity is defined. Solute mass fraction is set as zero.	$\bar{u}=\bar{u}_{in}$ $\omega=\omega_{in}=0$
Outlet	The concentration gradient is set as zero.	$\frac{\partial\omega}{\partial x_i}=0$
Wall (non-membrane)	Velocity and solute mass fraction gradient are set as zero.	$\bar{u}=\frac{\partial\omega}{\partial n}=0$
Membrane Surface	No permeation. Solute mass fraction is defined as 0.06.	$\bar{u}=0$ $\omega=\omega_w=0.06$
Rotating Disk	Set as moving, translational wall. The speed is relative to adjacent cell.	$n_{imp}=n_{rotation}$

2.4. Methodology of result analysis

As the mass transfer at the membrane surface is controlled by hydrodynamics, it is essential to quantify the mixing effectiveness. One of the ways to quantify the mixing effectiveness is by adopting the turbulent kinetic energy (k) as described in Equation (7). It is defined as the mean kinetic energy per unit mass of the transient components associated with eddies in turbulent flows which can be used as an indicator for measuring mixing effectiveness [10].

$$k=\frac{1}{2}\left(\overline{(u'_i)^2}+\overline{(u'_j)^2}+\overline{(u'_k)^2}\right) \tag{7}$$

where $u'=u-\bar{u}$.

The level of mixing at the membrane surface can be quantified using the mass transfer coefficient (k_{mt}) which can be expressed as in Equation (8).

$$k_{mt}=\frac{D}{\omega_w-\omega_b}\left(\frac{\partial\omega}{\partial n}\right)_w \tag{8}$$

where ω_w is the mass fraction of solute at the membrane surface and ω_b is the mass fraction of solute in the inlet bulk stream. It is worth noting that ω_b is zero when using the impermeable wall approach, so the only variable affecting k_{mt} is the solute mass fraction gradient in the y-direction $\left(\frac{\partial\omega}{\partial y}\right)_w$.

The proxy for fouling reduction can be approximated by wall shear stress (τ_w) [24, 27]**.** It shall be noted that the wall shear stress is directly proportional to shear rate (γ) under constant viscosity (μ) as shown in Equation (9). Therefore, any changes in shear rate $\left(\frac{\partial u}{\partial y}\right)$ is proportional to the changes in shear stress (τ_w) [28, 29].

$$\tau_w=\mu\gamma \tag{9}$$

It shall be noted that the shear rate and mass transfer coefficient were area-averaged (i.e., γ_{ave} and $k_{mt,ave}$). To evaluate the water flux in permeable membrane, the mass transfer coefficient for an impermeable wall ($k_{mt,imper}$) is first obtained from the CFD simulation to obtain the mass transfer coefficient under permeation conditions ($k_{mt,per}$) [30]:

$$\frac{k_{mt,per}}{k_{mt,imper}}=\psi+\left(1+0.26\psi^{1.4}\right)^{-1.7} \tag{10}$$

where ψ is defined as the volumetric flux divided by the impermeable mass transfer coefficient:

$$\psi=\frac{J}{\rho k_{mt,imp}} \tag{11}$$

Note that the correlation in Equation (11) is valid when the ψ < 20 [30]. The water flux (J) is determined based on the Kedem and Katchalsky model [31].

$$-\frac{J}{\rho}=-L_p\left(\Delta p_{tm}-\sigma\varphi R_{int}\omega_w\right). \tag{12}$$

where L_p is defined as membrane permeance, Δp_{tm} is denoted as the transmembrane pressure (Pa), σ is defined as reflection coefficient, R_{int} is membrane intrinsic rejection and φ is the osmotic pressure coefficient (Pa).

The mass balance on the membrane surface of feed side can be described using Equation (13):

$$J\omega_w=\rho D\left(\frac{\partial\omega}{\partial n}\right)_w+J\omega_p \tag{13}$$

Combining Equations (8), (12), (13), and the definition of the intrinsic rejection (R_{int}) gives a quadratic equation for ω_w as follows:

$$\omega_w=\omega_p+\frac{1}{2\sigma\varphi}\left(\Delta p_{tm}-\frac{k_{mt}}{L_p}\right)+\sqrt{\left[\frac{1}{2\sigma\varphi}\left(\Delta p_{tm}-\frac{k_{mt}}{L_p}\right)\right]^2+\frac{k_{mt}}{\sigma\varphi L_p}\left(\omega_b-\omega_p\right)}. \tag{14}$$

where the ω_p is the permeate solute concentration, σ is the reflection coefficient with value of 1, φ is the osmotic pressure coefficient (8.051×10^7 Pa), Δp_{tm} is the seawater transmembrane pressure at 2.94 MPa, k_{mt} is defined as the permeable wall mass transfer coefficient, L_p is the membrane permeance and ω_b is the bulk solute concentration. Hence, Equations (10) to (13) form a non-linear system that can be solved iteratively to determine the water flux (J) and permeable mass transfer coefficient ($k_{mt,per}$).

3. Mesh independence study

A mesh independence study was conducted to improve result accuracy and minimize numerical errors related to the computational mesh. Table 4 summarizes the number of elements and inflation layers generated to run the mesh independence study in this study. As shown in Fig. 2, our analysis

demonstrated that the results remained consistent above 7 million elements, indicating that further mesh refinement did not significantly affect the accuracy of the outcome. This outcome aligns with the general principle of mesh independence studies, where the aim is to find the point at which additional mesh refinement ceases to provide substantial improvements in accuracy. Therefore, 12.42 million mesh elements with 15 inflation layers near the membrane surface were used for the numerical simulation studies.

Table 4
Mesh independence study of different number of elements.

No. of Elements (× 10^6)	Number of Inflation layer
4.16	10
7.77	15
9.54	15
12.42	15

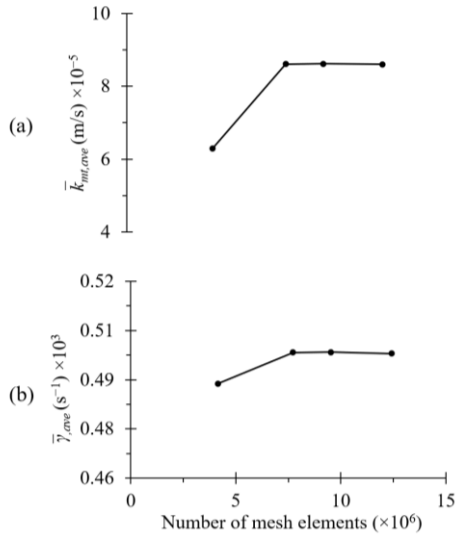

Fig. 2. Graph of the (a) mass transfer coefficient and (b) shear rate against number of elements

4. Validation of the models

Validation is a crucial step for ensuring a physical phenomenon is correctly modeled. It shall be noted that existing literature does not address the mass transfer solution at the membrane surface caused by stirring. However, it is possible to validate the flow solution against the theoretical result and other reference solutions from the literature.

For validation purpose, we have compared our data with the time-averaged wall shear rate $\left(\bar{\gamma}_{,ave}\right)$ formulation that is dependent on impeller rotation speed (n_{imp}) as reported by Bowen. This formulation is expressed as in Equation (15) [32]:

$$\gamma = 4.2 n_{imp}{}^{\alpha} \left(\frac{d_{imp}}{d_{tank}}\right)^{0.3} \frac{d_{imp}}{x_{imp}} \tag{15}$$

where n_{imp} is the rotation speed, α is the exponent of the rotation speed, d_{imp} is the diameter of impeller, d_{tank} is the diameter of tank and x_{imp} is the width of impeller.

The data points plotted using Equation (15) are compared against the CFD data in Fig. 3(b) in Section 5.1. Because of the absence of turbulent stress, Equation (15) gives a value of unity for the exponent of the n_{imp} (α = 1). However, for turbulent flow, the theoretical value of 1.5 for the exponent of n_{imp} (α = 1.5) can be obtained [29]. The exponent of n_{imp} obtained in this study has been compared against this theoretical value, as further discussed in Section 5.1.

5. Results & Discussion

5.1. Effect of shaft

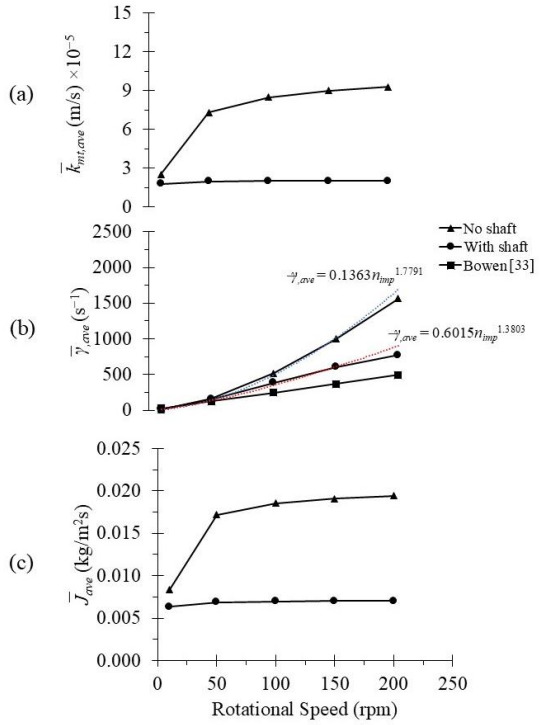

Fig. 3. Effect of the rotating speed on area-averaged (a) mass transfer coefficient and (b) wall shear at 30 L/h, and (c) water flux for cases with and without the shaft.

As shown in Fig. 3(b), it can be observed that the shear rate predicted using Equation (15) [32] is closer to the CFD data at a lower rotational speed (i.e., 10 rpm). This is because the turbulent intensity is smaller at lower rotational speed resulting in the wall shear computed via Equation (15) (see Section 4) to be closer to the current CFD prediction. This work also found that the exponent of the dependence of wall shear on the rotation speed for the cases with and without shaft are 1.78 and 1.38, respectively, which are close to the theoretical value of 1.5 as reported in the literature [29]. Fig. 3(a) and (c) show that $\bar{k}_{mt,ave}$ and $\bar{J}_{,ave}$ increase by about 73% as the disk rotational speed rises from 10 rpm to 200 rpm for the case without a shaft. This occurs because higher rotational speeds generate greater fluid velocity (Fig. 4), which enhances the disruption of the boundary layer on the membrane surface. Moreover, Fig. 3 reveals that as the rotational speed increases from 10 rpm to 200 rpm (for case without shaft), $\bar{\gamma}_{,ave}$ increases by approximately 200 times (Fig. 3b). These trends are supported by the local distribution of $\bar{\gamma}_{,ave}$ in Fig. 6, where a thicker zone of $\bar{\gamma}_{,ave}$ at the outer ring of the membrane surface was observed. The thicker zone of wall shear rate on the outer ring also agrees with observations reported by Movahedi and Jamshidi [11].

It is found that the hydrodynamics behavior of these two geometries possess significant difference when the rotational speed of the shaft increases (as in Fig. 3). From these findings, the difference in the prediction of $\bar{k}_{mt,ave}$ and $\bar{\gamma}_{,ave}$ between cases with shaft and without shaft increase significantly, at least doubling in magnitude as the disk rotational speed increases. This phenomenon can be explained by the pathline distribution as illustrated in Fig. 4. As displayed, the flow pathline in the stirred tank with shaft experienced a similar flow pattern at lower speed (10 rpm) compared to the tank without shaft. However, at a higher rotational speed of 200 rpm, the flow pathline movement of the stirred tank with shaft becomes more uniform and circular (see Fig. 4) caused by the high-speed circulating shaft, whereas a more non-uniform flow is observed for case without shaft. This flow non-uniformity augments the normal flow velocity across the membrane surface, as demonstrated by a stronger turbulent kinetic energy near the membrane surface for case without shaft, compared to case with shaft at a higher rotation speed (see Fig. 7.). Thus, a larger local wall shear and mass transfer distribution is observed for case without shaft compared to those predicted with shaft (see Fig. 6a and Fig. 6b).

Note that near the center of mixing tank, the hydrodynamics tends to be weaker (see Fig. 5 and Fig. 6). This results in a weaker mixing in the center

compared to the edge, where flow is more turbulent and chaotic due to the impeller action. Although the shaft plays a crucial role in connecting and supporting the impeller, it is indeed feasible to design an impeller without shaft, as demonstrated by various studies exploring different stirring mechanisms such as magnetic stirrer [33]. Such a design relies on magnetic force to suspend the impeller without the need for a connected shaft.

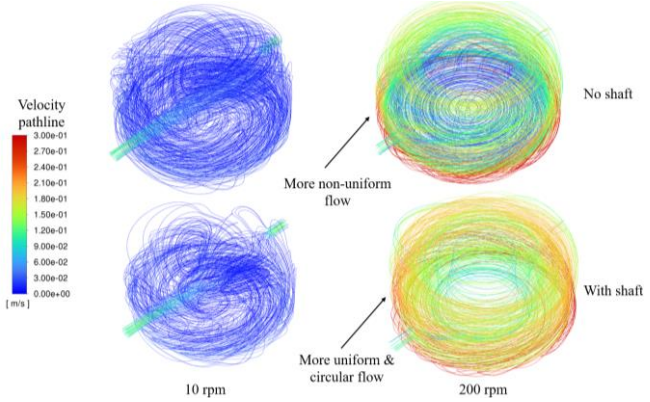

Fig. 4. Velocity pathline result of velocity for cases with and without shaft at different rotational speed.

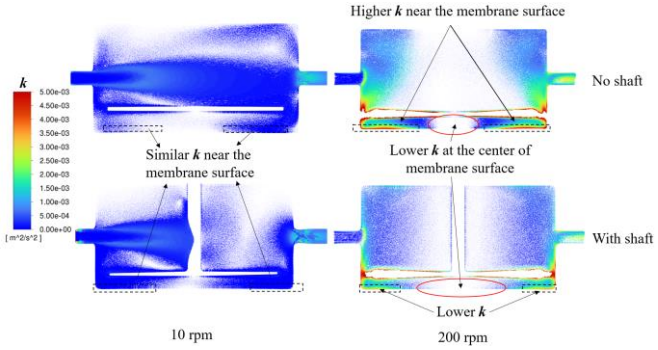

Fig. 5. Vector plot of turbulent kinetic energy on membrane wall for cases with and without shaft at different rotational speed.

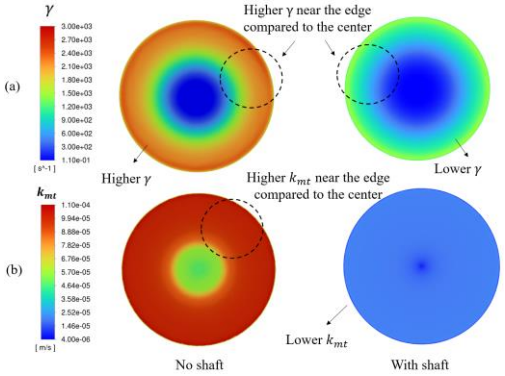

Fig. 6. Contour plot of the (a) wall shear rate and (b) mass transfer coefficient on membrane wall for cases with and without shaft at 200 rpm.

5.2. Effect of rotational direction

Table 5 reveals that the difference between mass transfer, wall shear and water flux are marginal regardless of whether the impeller rotates clockwise or anticlockwise. This similarity can be attributed to hydrodynamic conditions which are the primary factor contributing to the increase in mass transfer. While the velocity pathline pattern varies between the two cases (see Fig. 7), both cases still demonstrate a uniform and circular flow profile. The results show similar turbulence kinetic energy for both cases, as observed in Fig. 8. This similarity helps explain why mass transfer remains consistent across both rotational directions. As a result, this simplifies the operational decision-making, as the rotational direction becomes less significant in increasing both wall shear and mass transfer (see Fig. 9a and Fig. 9b).

Table 5
Results of mass transfer coefficient, wall shear rate and water flux for the cases of clockwise and anticlockwise rotation at 200 rpm.

Parameter	Clockwise	Anticlockwise
Mass transfer coefficient (k_{mt}), m/s	2.0364×10^{-5}	2.0362×10^{-5}
Wall shear rate (γ), s^{-1}	771.2	769.8
Water flux (J), kg/m^2s	7.0082×10^{-3}	7.0075×10^{-3}

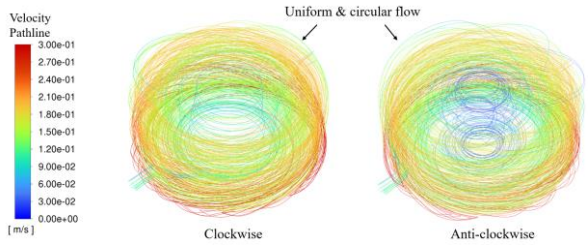

Fig. 7. Effect of rotational direction on velocity pathline for cases with clockwise and anticlockwise direction.

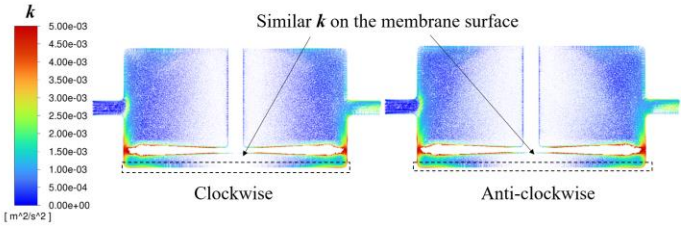

Fig. 8. Effect of rotational direction on turbulent kinetic energy for cases with clockwise and anticlockwise direction.

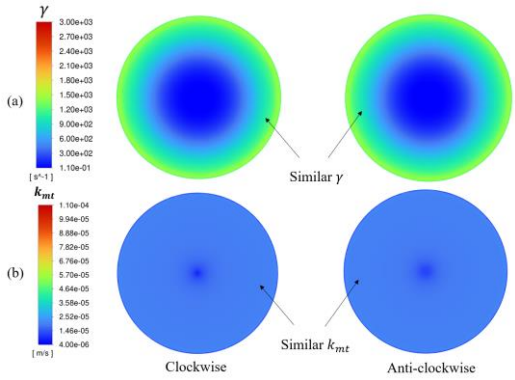

Fig. 9. Effect of direction on (a) wall shear rate and (b) mass transfer coefficient for cases with clockwise and anticlockwise direction

5.3. Effect of gap between rotating disk and membrane wall

Our findings reveal that $\overline{k}_{mt,ave}$, $\overline{\gamma}_{,ave}$ and $\overline{J}_{,ave}$ decreases by 11% (see Fig. 10a), 39% (see Fig. 10b) and 5.84% (see Fig. 10c) respectively as the gap ratio increases. This occurs because the local turbulent kinetic energy distribution near the membrane is more significant with smaller gap ratios (see Fig. 11), leading to improved mixing and mass transfer at the membrane surface. A smaller gap ratio reduces the quiescent region near the membrane, thereby enhancing the mass transfer. This explains why the case with a smaller gap ratio (G = 0.125) shows a thicker zone of high $\overline{k}_{mt,ave}$ and $\overline{\gamma}_{,ave}$ at the outer ring of bottom vessel compared to the case with larger gap ratio (G = 0.2) as shown in Fig. 12.

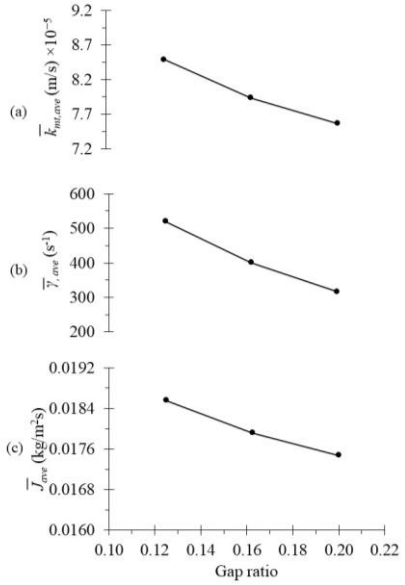

Fig. 10. Effect of gap ratio on area-averaged (a) mass transfer coefficient and (b) wall shear rate as well as (c) water flux at the same rotating speed of 100 rpm and inlet flow rate of 30 L/h.

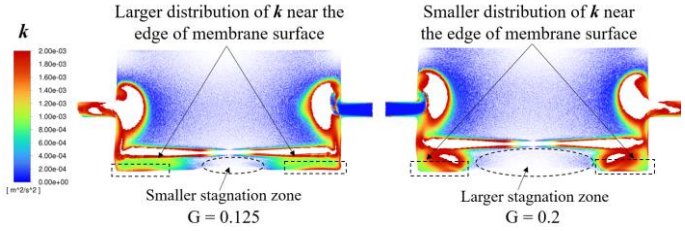

Fig. 11. Vector plot of turbulent kinetic energy at different gap ratio

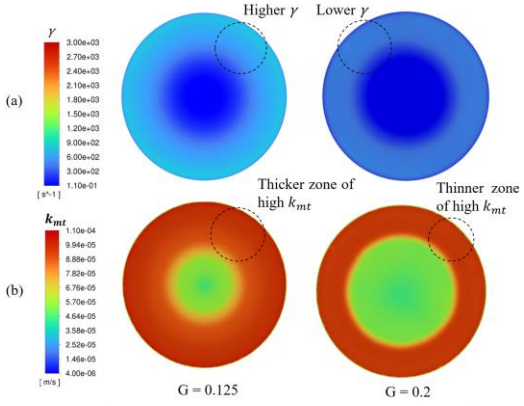

Fig. 12. Contour plot of the (a) wall shear rate and (b) mass transfer coefficient on membrane wall at different gap ratio.

6. Conclusion

In this research, 3D CFD simulations were used to examine the mass transfer and flow within a membrane tank with a rotating disk. Validation shows that the CFD results are in good agreement with theoretical solutions and reference data from the literature. The difference in the predictions of mass transfer coefficient, wall shear and water flux increase significantly when comparing cases with and without a shaft, potentially doubling in magnitude when the shaft is absent at higher disk rotational speed. This is because, at higher disk rotational speed, the flow in case with a shaft follows a more uniform and circular velocity pathline induced by the high-speed circulating shaft, whereas a more non-uniform flow pattern is observed in cases without a shaft. The importance of non-uniform flow is highlighted by its capacity to intensify the flow velocity perpendicular to the membrane surface, as evidenced by a stronger turbulent kinetic energy near the membrane surface for case without shaft (at a higher disk rotational speed). While the shaft typically plays a crucial role in connecting and supporting the impeller, it has been demonstrated by various studies, including those exploring magnetic stirring mechanisms, that designing an impeller without a shaft is possible.

The findings indicate that the rotational direction (clockwise vs. counterclockwise) does not significantly affect mass transfer, wall shear, or water flux. Additionally, a smaller gap between the membrane surface and the impeller reduces the quiescent region near the membrane, promoting stronger mixing and leading to enhanced mass transfer and water flux.

In this study, we have found that the shaft has significant impact on mixing near the membrane surface. Greater enhancement in membrane mass transfer could be achieved when considering flow generated by complex shape or impeller. Consequently, forthcoming research should prioritize this aspect.

Nomenclature

Symbol

D	Solute diffusivity (m^2/s)
g_{imp}	Gap between impeller and membrane surface (m)
g	Gravitational force (m/s^2)
G	Gap ratio
H	Height (m)
J	Water flux (m/s)
k	Turbulent kinetic energy (m^2/s^2)
k_{mt}	Mass transfer coefficient (m/s)
L_p	Membrane permeance (m/Pa.s)
n	Normal to the wall
n_{imp}	Rotational speed (rpm)
Q	Flow rate (L/h)
$R_{int}=\omega_p/\omega_w$	Membrane intrinsic rejection
r	Radius (m)
S_h	Sherwood number
t	Time (s)
$\bar{\boldsymbol{u}}$	Time-averaged velocity (m/s)
x_{imp}	Thickness (m)
x_i	Component of space coordinate

Greek letters

ρ	Density (kg/m^3)
μ	Dynamic viscosity (Pa.s)
τ_w	Wall shear stress (Pa)
ε	Viscous dissipation rate of turbulent kinetic energy (m^2/s^3)
δ_{ij}	Kronecker Delta function
σ	Reflection coefficient
φ	Osmotic pressure coefficient (Pa)
ω	Solute mass fraction
γ	Wall shear rate (s^{-1})

Subscript

b	Value at bulk conditions
imp	Value at impeller
tm	Value of transfer membrane pressure
per	Value for permeable membrane
$imper$	Value for impermeable membrane
in	Value at the domain inlet
out	Value at the domain outlet
w	Value at membrane wall conditions

Variables

$\bar{\phi}$	Time-averaged value
ϕ_{ave}	Area-averaged value

Acknowledgment

The corresponding author would like to thank University Malaysia Pahang Al-Sultan Abdullah for financial support under Internal Research grant RDU1803116.

Data availability

-

Declaration of competing interest

The authors declare that they have no known competing financial interests or personal relationships that could have appeared to influence the work reported in this paper.

Credit authorship contribution

C.E. Joey Vei: Methodology, Validation, Investigation, Writing – original draft.
Y.Y. Liang: Conceptualization, Investigation, Methodology, Validation, Resources, Writing – review & editing, Supervision, Project administration, Funding acquisition.
K.C. Ng: Methodology, Writing - review & editing.
Y.K. Chong: Methodology, Writing - review & editing.
J.X. Tan: Methodology, Writing - review & editing.
W.J. Lau: Writing – review & editing.

References

[1] P. Swapnil, M. Meena, The industrial development of polymeric membranes and membrane modules for reverse osmosis and ultrafiltration, Membrane-Based Hybrid Processes for Wastewater Treatment, Elsevier2021, pp. 1-12. https://doi.org/10.1016/b978-0-12-823804-2.00009-4.

[2] T.A. Saleh, V.K. Gupta, An Overview of Membrane Science and Technology, Nanomaterial and Polymer Membranes, Elsevier2016, pp. 1-23. https://doi.org/10.1016/b978-0-12-804703-3.00001-2.

[3] C.A. Serra, M.R. Wiesner, A comparison of rotating and stationary membrane disk filters using computational fluid dynamics, J. Membr. Sci. 165(1) (2000) 19-29. https://doi.org/10.1016/s0376-7388(99)00219-7.

[4] Y.K. Goi, Y.Y. Liang, W.J. Lau, G.A. Fimbres Weihs, Analysis of the effect of advanced FO spacer on the specific energy consumption of hybrid RO desalination system, J. Membr. Sci 668 (2023). https://doi.org/10.1016/j.memsci.2022.121247.

[5] H. Movahedi, S. Jamshidi, Experimental and CFD simulation of slurry flow in the annular flow path using two-fluid model, J. Pet. Sci. Eng. 198 (2021). https://doi.org/10.1016/j.petrol.2020.108224.

[6] C.A. Serra, M.R. Wiesner, J.-M. Laîné, Rotating membrane disk filters: design evaluation using computational fluid dynamics, Chem. Eng. J. 72(1) (1999) 1-17. https://doi.org/10.1016/s1385-8947(98)00128-4.

[7] M.M.A. Shirazi, A. Kargari, A.F. Ismail, T. Matsuura, Computational Fluid Dynamic (CFD) opportunities applied to the membrane distillation process: State-of-the-art and perspectives, Desalination 377 (2016) 73-90. https://doi.org/10.1016/j.desal.2015.09.010.

[8] Y.Y. Liang, G. Fimbres Weihs, R. Setiawan, D. Wiley, CFD modelling of unsteady electro-osmotic permeate flux enhancement in membrane systems, Chem. Eng. Sci. 146 (2016) 189-198. https://doi.org/10.1016/j.ces.2016.02.028.

[9] Y.Y. Liang, G.A. Fimbres Weihs, D.F. Fletcher, CFD study of the effect of unsteady slip velocity waveform on shear stress in membrane systems, Chem. Eng. Sci. 192 (2018) 16-24. https://doi.org/10.1016/j.ces.2018.07.009.

[10] K. Rana, D. Sarkar, Hydrodynamic study of the Single-Stirred Membrane Filtration Module: A CFD-based approach, Turk. J. Comput. Math. Educ. 11(3) (2020) 1854-1860. https://doi.org/10.17762/turcomat.v11i3.11899

[11] H. Movahedi, S. Jamshidi, New insight into hydrodynamic and cake erosion mechanism during rotating-disk dynamic microfiltration of concentrated bentonite suspensions at different salinity conditions, Sep. Purif. Technol. 300 (2022). https://doi.org/10.1016/j.seppur.2022.121844.

[12] J.-P. Torré, D.F. Fletcher, T. Lasuye, C. Xuereb, Single and multiphase CFD approaches for modelling partially baffled stirred vessels: Comparison of experimental data with numerical predictions, Chem. Eng. Sci. 62(22) (2007) 6246-6262. https://doi.org/10.1016/j.ces.2007.06.044.

[13] I. Ruigómez, E. González, P. Galán, J. Rodríguez-Sevilla, L. Vera, A Rotating Hollow Fiber Module for Fouling Control in Direct Membrane Filtration of Primary Settled Wastewater, Ind. Eng. Chem. Res. 58(36) (2019) 16901-16910. https://doi.org/10.1021/acs.iecr.9b02893.

[14] J.R. Rivero, L.R. Nemetz, M.M. Da Conceicao, G. Lipscomb, K. Hornbostel, Modeling gas separation in flat sheet membrane modules: Impact of flow channel size variation, Carbon Capture Sci. Technol. 6 (2023). https://doi.org/10.1016/j.ccst.2022.100093.

[15] J.E. Park, T.G. Kang, H. Moon, The Effect of the Rotating Disk Geometry on the Flow and Flux Enhancement in a Dynamic Filtration System, Membranes (Basel) 13(3) (2023). https://doi.org/10.3390/membranes13030291.

[16] S.S. Lee, A. Burt, G. Russotti, B. Buckland, Microfiltration of recombinant yeast cells using a rotating disk dynamic filtration system, Biotechnol. Bioeng. 48(4) (1995) 386-400. https://doi.org/10.1002/bit.260480411

[17] H. Ameur, Effect of the shaft eccentricity and rotational direction on the mixing characteristics in cylindrical tank reactors, Chin. J. Chem. Eng. 24(12) (2016) 1647-1654. https://doi.org/10.1016/j.cjche.2016.05.011.

[18] S. Wang, J. Wu, N. Ohmura, Inclined-Shaft Agitation for Improved Viscous Mixing, Ind. Eng. Chem. Res. 52(33) (2013) 11741-11751. https://doi.org/10.1021/ie401003s.

[19] K. Foo, Y.Y. Liang, G.A.F. Weihs, CFD study of the effect of SWM feed spacer geometry on mass transfer enhancement driven by forced transient slip velocity, J. Membr. Sci. 597 (2020). https://doi.org/10.1016/j.memsci.2019.117643.

[20] S.-Y. Tang, Y.-R. Qiu, Removal of copper(II) ions from aqueous solutions by complexation–ultrafiltration using rotating disk membrane and the shear stability of PAA–Cu complex, Chem. Eng. Res. Des. 136 (2018) 712-720. https://doi.org/10.1016/j.cherd.2018.06.030.

[21] L. Ding, M.Y. Jaffrin, J. Luo, Dynamic Filtration with Rotating Disks, and Rotating or Vibrating Membranes, Progress in Filtration and Separation2015, pp. 27-59. https://doi.org/10.1016/b978-0-12-384746-1.00002-1.

[22] D. Sarkar, D. Datta, D. Sen, C. Bhattacharjee, Simulation of continuous stirred rotating disk-membrane module: An approach based on surface renewal theory, Chem. Eng. Sci. 66(12) (2011) 2554-2567. https://doi.org/10.1016/j.ces.2011.02.056.

[23] P. Velex, International Gear Conference 2014: 26th–28th August 2014, Lyon, 2014. https://doi.org/10.1016/c2013-0-23221-9.

[24] Y.K. Chong, Y.Y. Liang, W.J. Lau, G.A. Fimbres Weihs, 3D CFD study of hydrodynamics and mass transfer phenomena for spiral wound membrane submerged-type feed spacer with different node geometries and sizes, Int. J. Heat Mass Transfer 191 (2022). https://doi.org/10.1016/j.ijheatmasstransfer.2022.122819.

[25] V. Geraldes, M.D. Afonso, Generalized mass-transfer correction factor for nanofiltration and reverse osmosis, AlChE J. 52(10) (2006) 3353-3362. https://doi.org/10.1002/aic.10968.

[26] K.Y. Toh, Y.Y. Liang, W.J. Lau, D.F. Fletcher, CFD study of the effect of perforated spacer on pressure loss and mass transfer in spacer-filled membrane channels, Chem. Eng. Sci. 222 (2020). https://doi.org/10.1016/j.ces.2020.115704.

[27] K. Foo, Y.Y. Liang, C.K. Tan, G.A. Fimbres Weihs, Coupled effects of circular and elliptical feed spacers under forced-slip on viscous dissipation and mass transfer enhancement based on CFD, J. Membr. Sci 637 (2021). https://doi.org/10.1016/j.memsci.2021.119599.

[28] R. Bian, K. Yamamoto, Y. Watanabe, The effect of shear rate on controlling the concentration polarization and membrane fouling, Desalination 131(1-3) (2000) 225-236. https://doi.org/10.1016/s0011-9164(00)90021-3.

[29] J.A. Sánchez Pérez, E.M. Rodríguez Porcel, J.L. Casas López, J.M. Fernández Sevilla, Y. Chisti, Shear rate in stirred tank and bubble column bioreactors, Chem. Eng. J. 124(1-3) (2006) 1-5. https://doi.org/10.1016/j.cej.2006.07.002.

[30] V. Geraldes, M.D. Afonso, Generalized mass - transfer correction factor for nanofiltration and reverse osmosis, AlChE J. 52(10) (2006) 3353-3362. https://doi.org/10.1002/aic.10968.

[31] O. Kedem, A. Katchalsky, Thermodynamic analysis of the permeability of biological membranes to non-electrolytes, Biochim. Biophys. Acta 27(2) (1958) 229-46. https://doi.org/10.1016/0006-3002(58)90330-5.

[32] R.L. Bowen, Unravelling the mysteries of shear-sensitive mixing systems, Chemical Engineering 93 (1986) 55-63.

[33] S. Salisu, Design and Fabrication of a Magnetic Stirrer for Bio-Diesel Production, FUPRE Journal of Scientific and Industrial Research (FJSIR) 4(1) (2020) 36-49. https://doi.org/10.1016/j.sjbs.2020.11.034